

Supporting Information

Ultrathin 2D NiCo-LDH nanosheet decorated NH₂-UiO-66 MOF-nanocomposite with exceptional chemical stability for electrocatalytic water splitting

Saddam Sk,^[a,b] Ragunath Madhu,^[b,c] Deepak S. Gavali,^[d] Vidha Bhasin,^[e] Ranjit Thapa,^[d]
Shambhu Nath Jha,^[e] Dibyendu Bhattacharyya,^[e] Subrata Kundu,^[b,c]* Ujjwal Pal^[a,b]*

[a] Department of Energy & Environmental Engineering, CSIR-Indian Institute of Chemical Technology, Hyderabad-500007, India.

[b] Academy of Scientific and Innovative Research (AcSIR), Ghaziabad-201002, India.

[c] Electrochemical Process Engineering (EPE) Division, CSIR-Central Electrochemical Research Institute (CECRI), Karaikudi-630003, Tamil Nadu, India.

[d] Department of Physics, SRM University AP, Amaravati 522240, Andhra Pradesh, India.

[e] Atomic and Molecular Physics Division, Bhabha Atomic Research Centre, Mumbai 400085, India.

*Corresponding author: upal03@gmail.com, ujjwalpal@iict.res.in (U. Pal);
kundu.subrata@gmail.com, skundu@cecri.res.in (S. Kundu)

Table of Content

Content	Page No.
Methods	3
Preparation of integrated catalyst	4
Figure S1. Snapshot of the as-synthesized sample	4
Characterizations	5
Table S1. Structural parameters obtained from N ₂ adsorption isotherms analysis	6
X-ray Absorption Spectroscopy (XAS) Measurement	6-7
Table S2. Co, Ni, and Zr K edge EXAFS Fitting results	8
Computational Details	8
Electrochemical measurements	9
Table S3. Loading of the corresponding catalyst over a nickel foam substrate for OER and HER process	9
Table S4. Comparison of NiCo-LDH@NH ₂ -UiO-66 based electrocatalyst with our catalyst for OER application in 1 M KOH electrolyte solution. (CC- Carbon cloth; NF-	9

Nickel foam)	
Table S5. Comparison of NiCo-LDH@NH ₂ -UiO-66 based electrocatalyst with our catalyst for HER application in 1 M KOH electrolyte solution. (CC-Carbon cloth; NF-Nickel foam)	10
Figure S2. AFM topography and corresponding hight profile of the (a) NiCo-LDH, (b) NH ₂ -UiO-66, and (c) NiCo-LDH@NH ₂ -UiO-66.	11
Figure S3. SEM images of (a) NH ₂ -UiO-66, (b) NiCo-LDH; and FE-SEM images of (c) NiCo-LDH, (d) NiCo-LDH@NH ₂ -UiO-66.	12
Figure S4. TEM images of the (a, b) NiCo-LDH, and (d, e) NiCo-LDH@NH ₂ -UiO-66; and HR-TEM image of the (c) NiCo-LDH, and (f) NiCo-LDH@NH ₂ -UiO-66.	13
Figure S5. HR-TEM image of the (a) NiCo-LDH, and (b) NiCo-LDH@NH ₂ -UiO-66.	13
Figure S6. (a, b) HAADF image, (c-e) elemental mapping of NiCo-LDH.	14
Figure S7. Line profile of NiCo-LDH@NH ₂ -UiO-66.	14
Figure S8. EDX profile of NiCo-LDH@NH ₂ -UiO-66.	15
Figure S9. (a-c) N ₂ adsorption-desorption isotherms, (d-f) pore size distribution curves of the as-synthesized NH ₂ -UiO-66, NiCo-LDH, and NiCo-LDH@NH ₂ -UiO-66 catalysts.	16
Figure S10. TGA curves under a flow of N ₂ at a heating rate of 10 °C min ⁻¹ .	17
Figure S11. (a) XPS full scan survey spectra of the as-synthesized catalysts. High resolution XPS spectra of (b) Zr 3d, (c) Co 2p, (d) Ni 2p, (e) N 1s, (f) C 1s, and (g) O 1s of NH ₂ -UiO-66, NiCo-LDH, and NiCo-LDH@NH ₂ -UiO-66 catalyst.	18
Figure S12. Represents the pH dependent electrocatalytic activity of NiCo-LDH@NH ₂ -UiO-66 catalyst towards OER at four different pH~13.0, 13.4, 13.6, 14 condition.	19
Figure S13. Chronocoulometric study of NiCo-LDH@NH ₂ -UiO-66 catalyst for 2h towards OER in 1 M KOH.	19
Figure S14. (a-c) are the reduction area peaks for NH ₂ -UiO-66, NiCo-LDH and NiCo-LDH@NH ₂ -UiO-66, respectively.	20
Figure S15. The LSV polarization results of NiCo-LDH@NH ₂ -UiO-66 catalyst performed in a carbon cloth (CC) substrate.	21
Figure S16. Represents the pH dependent electrocatalytic activity of NiCo-LDH@NH ₂ -UiO-66 catalyst towards HER at four different pH~13.0, 13.4, 13.6, 14	21

environment.	
Figure S17. Chronocoulometric study of NiCo-LDH@NH ₂ -UiO-66 catalyst for 2h towards HER in 1 M KOH.	22
Figure S18. (a) LSV curve of acceleration degradation (AD) study after 1000 cycles for HER, (b) corresponding EIS spectra in 1 M KOH electrolyte solution.	22
Figure S19. XRD analysis of NiCo-LDH@NH ₂ -UiO-66 catalyst after electrocatalytic HER and OER process.	23
Figure S20. FE-SEM images of NiCo-LDH@NH ₂ -UiO-66 catalyst after electrocatalytic (a, b) OER and (c, d) HER process in 1 M KOH electrolyte solution.	23
Figure S21. XPS spectra of NiCo-LDH@NH ₂ -UiO-66 catalyst before and after electrocatalytic HER and OER: (a) full scan survey spectra, (b) Zr 3d, (c) Co 2p, (d) Ni 2p, (e) N 1s, (f) C 1s, and (g) O 1s.	24
Reference	25-26

Methods

Materials and reagents: All of the chemicals were commercially available and used without further purification: N, N-Dimethylformamide (DMF, Finar Chemicals), Zirconium (IV) tetrachloride (ZrCl₄, Sigma-Aldrich), 2-Aminoterephthalic acid (NH₂-BDC, Sigma-Aldrich), glacial acetic acid (CH₃COOH, Finar Chemicals), Methanol (MeOH, Finar Chemicals), 2-methylimidazole (MIM, Sigma-Aldrich), Nickel (II) nitrate hexahydrate [Ni(NO₃)₂·6H₂O, Sigma-Aldrich], and Cobalt(II) nitrate hexahydrate (Co(NO₃)₂·6H₂O, Sigma-Aldrich). In all the experiments distilled water (DI H₂O) was used. Sonication (GT Sonic 50 Hz) and centrifugation (REMI, 50 Hz) were used for re-dispersing and separation of the catalysts, respectively.

Preparation of integrated catalyst

Preparation of NH₂-UiO-66

NH₂-UiO-66 prepared through a facile solvothermal treatment.¹ Typically, 5 mL DMF solution of ZrCl₄ (10.20 mg, 8.75 mM), and 5 mL DMF solution of NH₂-BDC (14.50 mg, 8.01 mM) were mixed in small RB. Following that, 1.2 mL CH₃COOH was added, and then transferred into a Teflon liner stainless-steel autoclave. The autoclave was sealed and heated at 120 °C for 12 h. The product was collected by centrifugation and washed three times with

DMF, and then sequentially immersed in MeOH for 24 h. Finally, NH₂-UiO-66 was activated by removing the solvent under vacuum for 12 h at 50 °C.

Preparation of ultrathin NiCo-LDH Nanosheet Arrays and NiCo-LDH@NH₂-UiO-66 heterostructure catalyst

Ultrathin NiCo-LDH nanosheet arrays with a ratio of Ni/Co = 1:1 precursor were prepared by a facile solvothermal method.² In a typical procedure, a precursor solution containing 40 mM MIM, 10 mM Ni(NO₃)₂·6H₂O, and 10 mM Co(NO₃)₂·6H₂O in 40 mL of MeOH was first prepared under vigorous magnetic stirring for 10 min. After this, the solution was transferred into a Teflon liner stainless-steel autoclave. The autoclave was sealed and heated at 110 °C for 14 h. After the autoclave cooled to room temperature, the as-prepared sample was taken out and washed in MeOH under sonication for 2 min to remove the residual compound. Finally, the sample was at 80 °C for 10 h.

The following reaction has been followed for integrating the highly efficient catalyst. Similarly, NiCo-LDH@NH₂-UiO-66 heterostructure material was prepared also using the above same methodology by adding a certain amount of as-prepared NH₂-UiO-66 into the precursor solution of NiCo-LDH.



Figure S1. Snapshot of the as-synthesized sample.

Characterizations

The structural phase analysis of the as-synthesized catalysts was performed by using Powder X-ray diffraction patterns (XRD) on a Bruker AXS diffractometer (D8 advance) at a generator voltage of 40 kV and current of 30 mA using Cu-K α ₁ irradiation ($\lambda = 1.5406 \text{ \AA}$). The sample was scanned in the range of $2\theta = 10\text{-}80^\circ$ with a scan rate of 1 s/step. X-ray photoelectron spectroscopy (XPS) was performed via a Kratos (axis 165) analytical instrument with Mg K α irradiation. About 10⁻⁹ Torr pressure was maintained in the

spectrometer. The structural morphology of the catalysts was examined by using MIRA3 FE-SEM (TESCAN) Scanning electron microscopy (SEM) at an accelerating voltage of 5 kV. Transmission electron microscopy (TEM) image of the representative catalysts was obtained by using a JEOL 2010EX TEM instrument equipped with the high-resolution style objective-lens pole piece at an acceleration voltage of 200 kV fitted with a CCD camera. Atomic force microscopy (AFM) images were acquired using TM 3D ADC5 multimode (NX10, Park systems) in tapping mode to measure the thickness of the materials. ATR-IR spectroscopy was used to characterize the surface feature of the particles. The spectra were acquired using a Perkin Elmer ATR-IR spectrometer. A small drop of the test sample was placed on the smart gate surface over wave numbers ranging from 4000 to 650 cm^{-1} . The catalysts were characterized by Raman spectroscopy (Horiba Jobin-Yvon Lab Ram HR, Japan) using 633 nm He-Ne laser. The spectra were recorded by spreading about 10 mg of solid sample over a glass slide kept under microscope. N_2 adsorption-desorption isotherms of the catalysts were obtained on a Quantachrome Nova 2200e gas adsorption analyzer at 77 K. Thermogravimetric analyses (TGA) of the samples were carried out using the TA Instruments SDT Q600 apparatus to study the thermal treatment. Around 12-15 mg of the sample was placed in the TG pan and was heated at a scan rate of 10 $^\circ\text{C min}^{-1}$ within a temperature range of 25 to 900 $^\circ\text{C}$ and under an inert atmosphere of N_2 gas flow of 50 ml min^{-1} . Inductively coupled plasma-optical emission spectroscopy (ICP-OES) was carried out using a Perkin-Elmer ICP-OES chemical analyzer. The sample was first dissolved in aqua regia at 70 $^\circ\text{C}$ for 30 min. Then, the solution was transferred and diluted to 100 ml in the volumetric flask. Finally, the obtained solution was analysed on the ICP-OES.

Table S1. Structural parameters obtained from N_2 adsorption isotherms analysis.

Samples	S_{BET} ($\text{m}^2 \text{g}^{-1}$) ^a	Pore volume ($\text{cm}^3 \text{g}^{-1}$) ^b	Average pore size (nm) ^b
$\text{NH}_2\text{-UiO-66}$	668.7	0.43	2.55
NiCo-LDH	25.5	0.17	26.21
NiCo-LDH@ $\text{NH}_2\text{-UiO-66}$	276.6	0.37	5.35

a. Obtained from BET method.

- b. Total pore volume taken from the N₂ adsorption volume at a relative pressure (P/P₀) of 0.99.

X-ray Absorption Spectroscopy (XAS) Measurement

X-ray Absorption Spectroscopy (XAS) measurement of NiCo-LDH@NH₂-UiO-66 sample has been carried out at Ni, Co and Zr K edge in transmission mode at the Scanning EXAFS Beamline (BL-9) at the Indus-2 Synchrotron Source (2.5 GeV, 200 mA) at the Raja Ramanna Centre for Advanced Technology (RRCAT), Indore, India.^{3, 4} The beamline uses a double crystal monochromator (DCM) which works in the photon energy range of 4-25 KeV with a resolution of 10⁴ at 10 KeV. A 1.5 m horizontal pre-mirror with meridional cylindrical curvature is used before the DCM for collimation of the beam and higher harmonic rejection. The second crystal of the DCM is a sagittal cylinder with a radius of curvature in the range of 1.28 - 12.91 meters which provides horizontal focusing to the beam while another Rh/Pt coated bendable post mirror facing down is used for vertical focusing of the beam at the sample position.

For the transmission mode measurement, three ionization chambers (300 mm in length each) have been used for data collection, one ionization chamber for measuring incident flux (I_0), the second one for measuring transmitted flux (I_t) and the third ionization chamber for measuring XAS spectrum of a reference metal foil for energy calibration. Appropriate gas pressure and gas mixtures have been chosen to achieve 10-20% absorption in the first ionization chamber and 70-90% absorption in the second ionization chamber to improve the signal-to-noise ratio. The absorption coefficient μ is obtained using the relation:

$$I_t = I_0 e^{-\mu x}$$

where x is the thickness of the absorber.

The EXAFS spectra have been extracted using the standard procedure.⁵⁻⁷ To take care of the EXAFS oscillations in the absorption spectra, the energy-dependent absorption coefficient $\mu(E)$ has been converted to absorption function $\chi(E)$ defined as follows:

$$\chi(E) = \frac{\mu(E) - \mu_0(E)}{\Delta\mu_0(E_0)}$$

where E_0 absorption edge energy, $\mu_0(E_0)$ is the bare atom background and $\Delta\mu_0(E_0)$ is the step in the $\mu(E)$ value at the absorption edge. After converting the energy scale to the photoelectron wave number scale (k) as defined by:

$$k = \sqrt{\frac{2m(E - E_0)}{\hbar^2}}$$

the energy-dependent absorption coefficient $\chi(E)$ has been converted to the wave number-dependent absorption coefficient $\chi(k)$, where m is the electron mass. Finally, $\chi(k)$ is weighted by k^2 to amplify the oscillation at high k and the functions $\chi(k)k^2$ are Fourier transformed in r space to generate the $\chi(r)$ versus r plots (or FT-EXAFS spectra) in terms of the real distances from the centre of the absorbing atom. The k range used for Fourier transform is 2-10 Å⁻¹. The ATHENA subroutine available within the Demeter software package⁸ has been used for background reduction and Fourier transform to derive the $\chi(r)$ versus r plots from the absorption spectra.

To extract quantitative information regarding the local structure surrounding the Co, Ni and Zr sites in the samples, the experimental plots have been fitted with theoretically generated FT-EXAFS spectra. For the generation of the theoretical EXAFS spectra starting from an assumed model of the sample structure, the ATOMS subroutine has been used and finally fitting of experimental data with the theoretical spectra has been carried out using the ARTEMIS subroutine available within the Demeter package.⁸ During the fitting, bond distances and disorder (Debye-Waller) factors (σ^2), which give the mean square fluctuations in the distances, have been used as fitting parameters. The coordination number has been kept fixed at the values obtained from the respective CIF files of the samples as supplied by the user. The goodness of fit has been determined by the value of the R_{factor} defined by:

$$R_{factor} = \sum \frac{[\text{Im}(\chi_{dat}(r_i) - \chi_{th}(r_i))]^2 + [\text{Re}(\chi_{dat}(r_i) - \chi_{th}(r_i))]^2}{[\text{Im}(\chi_{dat}(r_i))]^2 + [\text{Re}(\chi_{dat}(r_i))]^2}$$

where, χ_{dat} and χ_{th} refer to the experimental and theoretical $\chi(r)$ values respectively and Im and Re refer to the imaginary and real parts of the respective quantities.

Table S2. Co, Ni, and Zr K edge EXAFS Fitting results

Co Edge					
	N	σ^2	R (Å)	R_{factor}	Edge energy(eV)
Co-O	6	0.0054 ±0.0034	2.03±0.02	0.0077074	7721.82

Co-Ni/Co	6	0.0040 ±0.0007	3.04±0.01		
Ni Edge					
	N	σ^2	R (Å)	R_{factor}	Edge energy(eV)
Ni-O	6	0.0013 ±0.0004	2.02±0.01	0.0061563	8345.66
Ni-Co/Ni	6	0.0014 ±0.0004	3.13±0.01		
Zr Edge					
	N	σ^2	R (Å)	R_{factor}	Edge energy(eV)
Zr-O	2	0.0030 ±0.0028	2.07±0.03	0.0022323	18005.40
Zr-O	6	0.0040 ±0.0038	2.22±0.04		

Computational Details

We have executed the density functional theory (DFT) based calculation using Vienna Ab initio Simulation Package (VASP).⁹ The interaction between electron and ion is defined by the projector-augmented wave (PAW) potential method and exchange-correlation energy was defined by Perdew, Burke, and Ernzerhof (PBE).^{10, 11} For all the geometry optimization calculations, we have used kinetic energy cutoff of 450 eV, where the convergence criteria for total energy and force convergence are defined as 10^{-5} eV per atom and 0.001 eV/Å, respectively. The long-range Van-der-Waal's interaction between surfaces and atom/ion was defined by Grimme's (DFT-D2) method.¹² To avoid the interaction between the layers, a 15 Å vacuum is used along the z-axis.

Electrochemical measurements

The electrochemical workstation AURT-M204 was used for the entire OER studies. A typical three electrode set-up was employed for OER experiments. Hg/HgO as reference electrode, graphite rod as the counter electrode and Nickel Foam (NF) working electrode were purchased from CH instruments. DI water was used throughout the entire experimental analysis. At first, the NF of dimension 4×0.5 cm² was cleaned with 2 M HCl and H₂O: EtOH mixture, acetone and dried in a hot air oven. After that catalytic ink was prepared by

using the PVDF (polyvinylidene fluoride) as binder and uniformly coated over the NF. Then the coated sample was kept for drying at 60 °C in a hot air oven. Then the modified electrode sample was used as working electrode for OER, HER and TWS process. All reported potentials were calibrated versus the reversible hydrogen electrode (RHE) using the equation of $E_{\text{RHE}} = E_{\text{Hg/HgO}} + (0.098 + 0.059 \times \text{pH}) \text{ V}$, where E_{RHE} is the potential referred to RHE and $E_{\text{Hg/HgO}}$ is the measured potential against the Hg/HgO reference electrode.

Table S3. Loading of the corresponding catalyst over a nickel foam substrate for OER and HER process

Sl. No	Name of the catalyst	Catalyst loading for OER	Catalyst loading for HER
1	NH ₂ -UiO-66	1.12	1.06
2	NiCo-LDH	1.1	0.98
3	NiCo-LDH@NH ₂ -UiO-66	1.08	1.05

Table S4. Comparison of NiCo-LDH@NH₂-UiO-66 based electrocatalyst with our catalyst for OER application in 1 M KOH electrolyte solution. (CC- Carbon cloth; NF- Nickel foam)

Sl. No	Electrocatalyst	Substrate	Overpotential (mV)	Current density (mA cm ⁻²)	Ref.
1	NiCo-LDH/NiCo ₂ S ₄	CC	254	50	13
2	NiCo-LDH	NF	271	10	14
3	Co ₃ O ₄ @NiCo LDH	NF	279	10	15
4	Co ₉ S ₈ @NiCo-LDH	NF	278	30	16
5	Co ₃ S ₄ @NiCo-LDH	NF	262	100	17
6	MoS ₂ /NiCo ₂ S ₄	NF	220	10	18

7	NiCo-LDH@NiCoP	NF	219	10	19
8	Ni ₃ S ₂ /Cu–NiCo LDH	NF	218	100	20
9	Ce ³⁺ doped NiCo–LDH	NF	250	50	21
10	V doped NiCo-LDH	CC	280	10	22
11	NiCo-LDH@NH ₂ -UiO-66	NF	296	50	This work

Table S5. Comparison of NiCo-LDH@NH₂-UiO-66 based electrocatalyst with our catalyst for HER application in 1 M KOH electrolyte solution. (CC-Carbon cloth; NF-Nickel foam)

Sl. No	Electrocatalyst	Substrate	Overpotential (mV)	Current density (mA cm ⁻²)	Ref.
1	NiCo-LDH/NiCo ₂ S ₄	CC	219	50	13
2	NiCo-LDH	NF	162	10	14
3	Co ₃ O ₄ @NiCo LDH	NF	113	10	15
4	Co ₉ S ₈ @NiCo-LDH	NF	168	10	16
5	Co ₃ S ₄ @NiCo-LDH	NF	210	50	17
6	MoS ₂ /NiCo ₂ S ₄	NF	90	10	18
7	NiCo-LDH@NiCoP	NF	112	10	19
8	Ni ₃ S ₂ /Cu–NiCo LDH	NF	304	100	20

9	Ce ³⁺ doped NiCo-LDH	NF	134	50	21
10	NiCo-LDH@NH ₂ -UiO-66	NF	224	50	This work

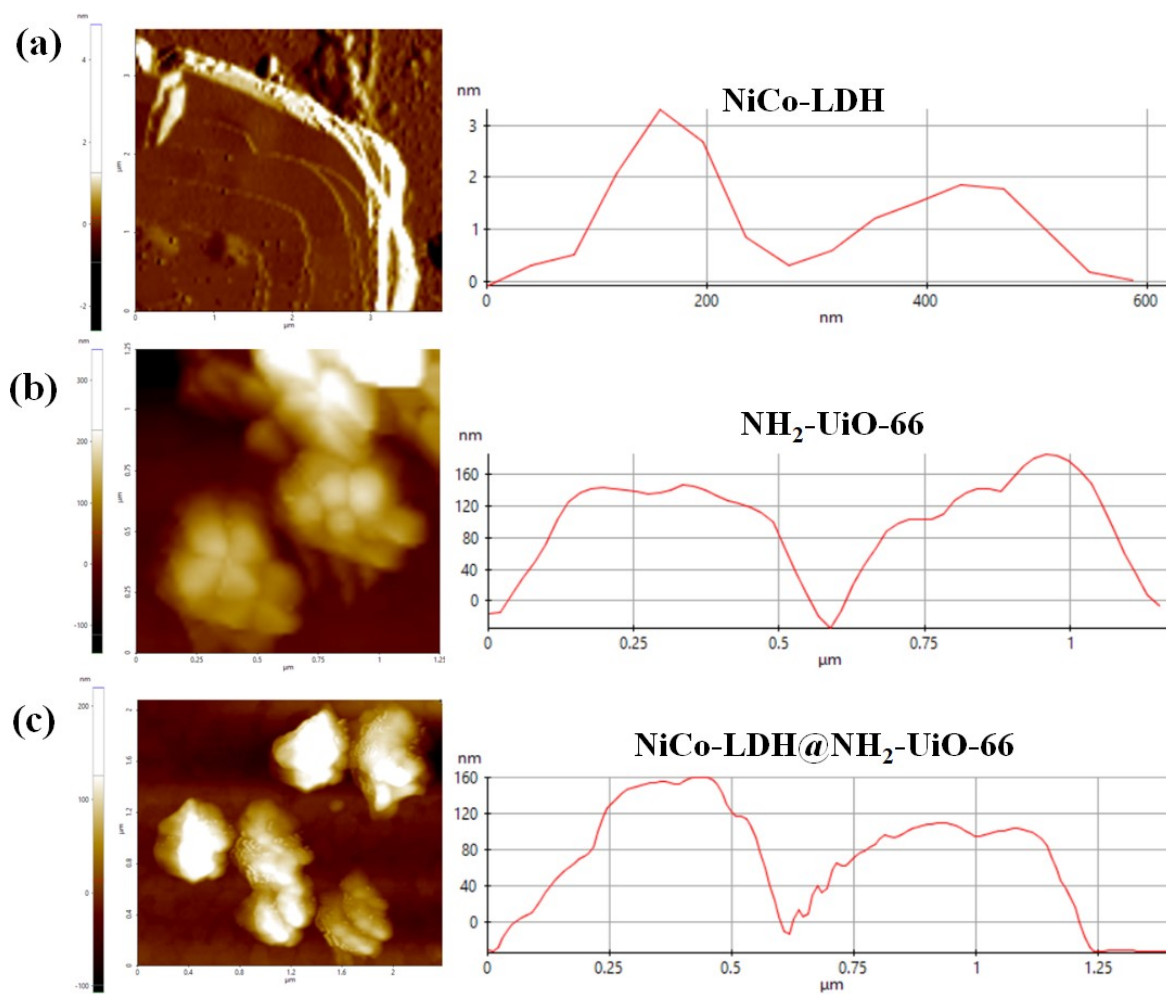


Figure S2. AFM topography and corresponding height profile of the (a) NiCo-LDH, (b) NH₂-UiO-66, and (c) NiCo-LDH@NH₂-UiO-66.

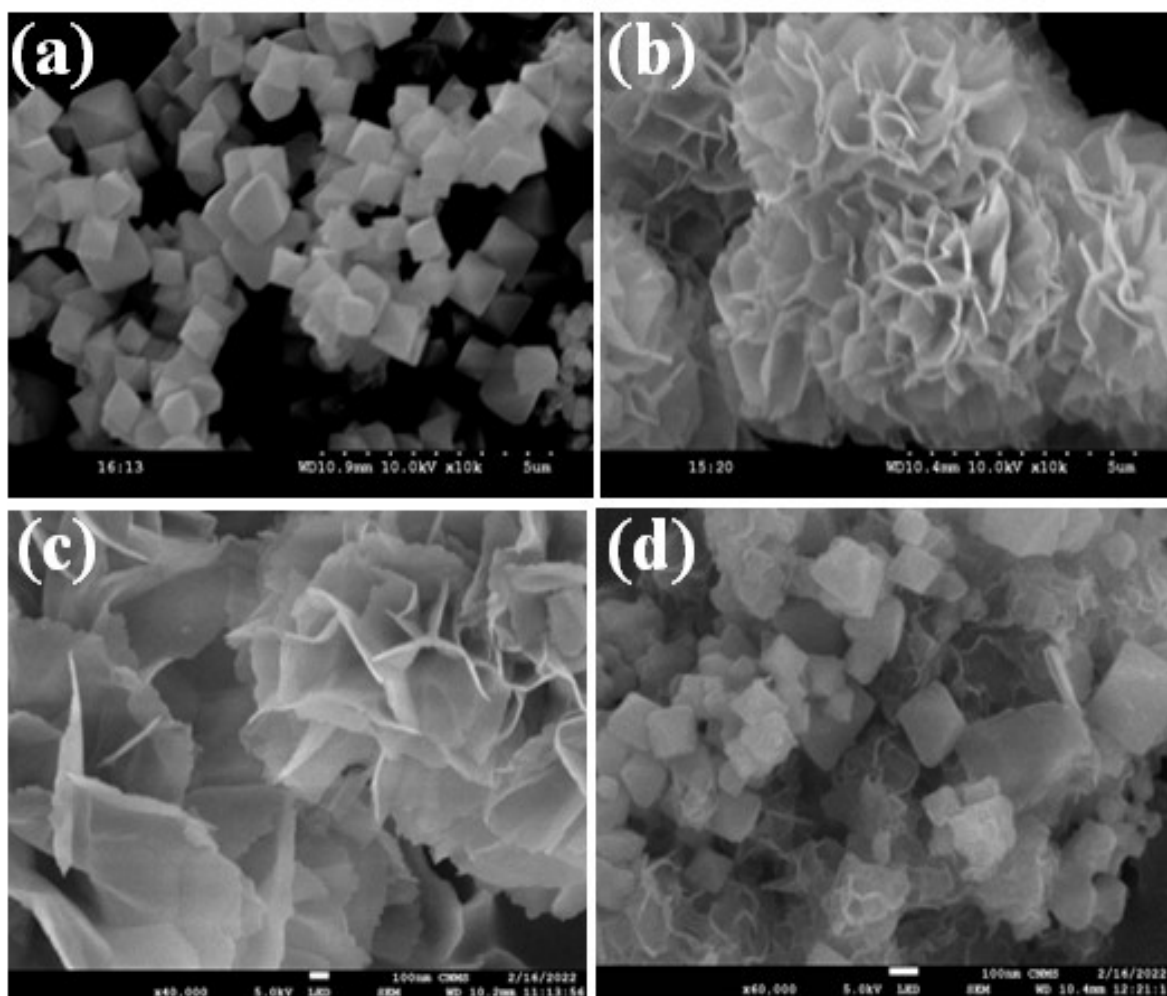


Figure S3. SEM images of (a) $\text{NH}_2\text{-UiO-66}$, (b) NiCo-LDH ; and FE-SEM images of (c) NiCo-LDH , (d) $\text{NiCo-LDH@NH}_2\text{-UiO-66}$.

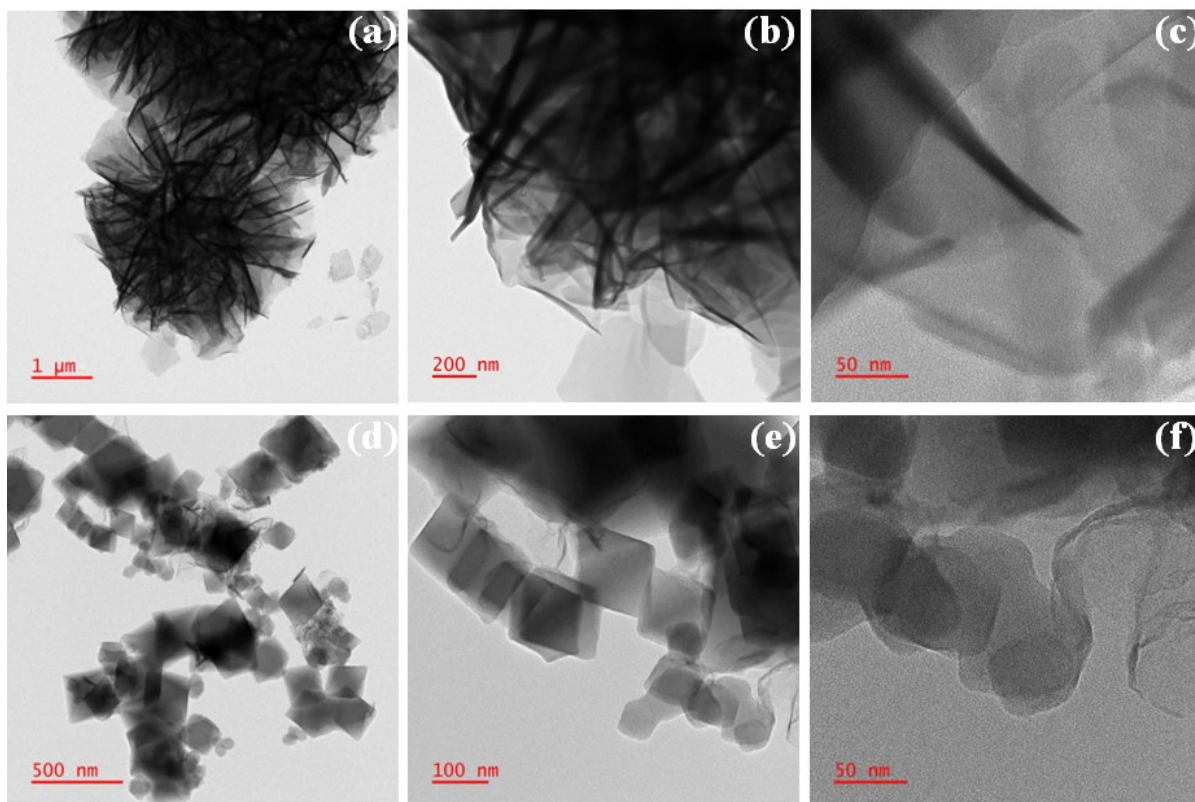


Figure S4. TEM images of the (a, b) NiCo-LDH, and (d, e) NiCo-LDH@NH₂-UiO-66; and HR-TEM image of the (c) NiCo-LDH, and (f) NiCo-LDH@NH₂-UiO-66.

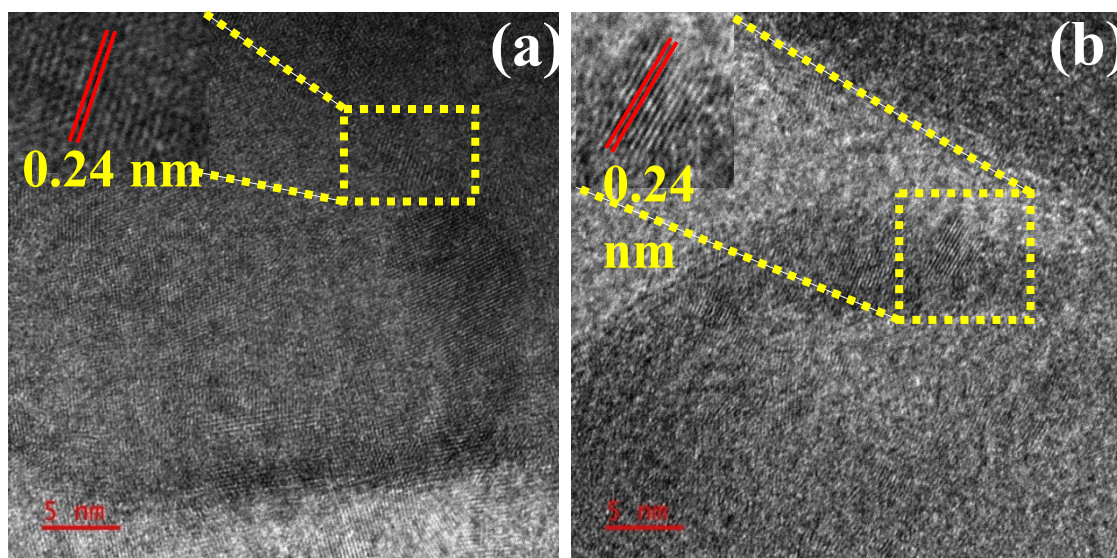


Figure S5. HR-TEM image of the (a) NiCo-LDH, and (b) NiCo-LDH@NH₂-UiO-66.

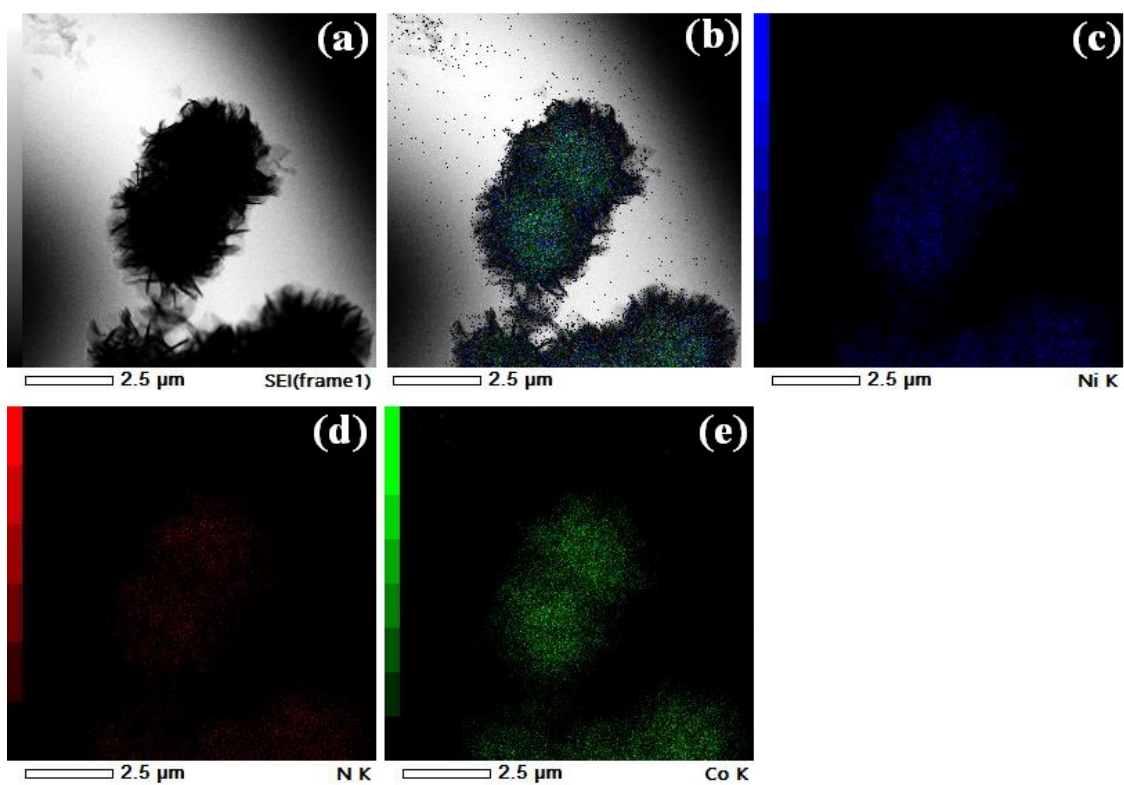


Figure S6. (a, b) HAADF image, (c-e) elemental mapping of NiCo-LDH.

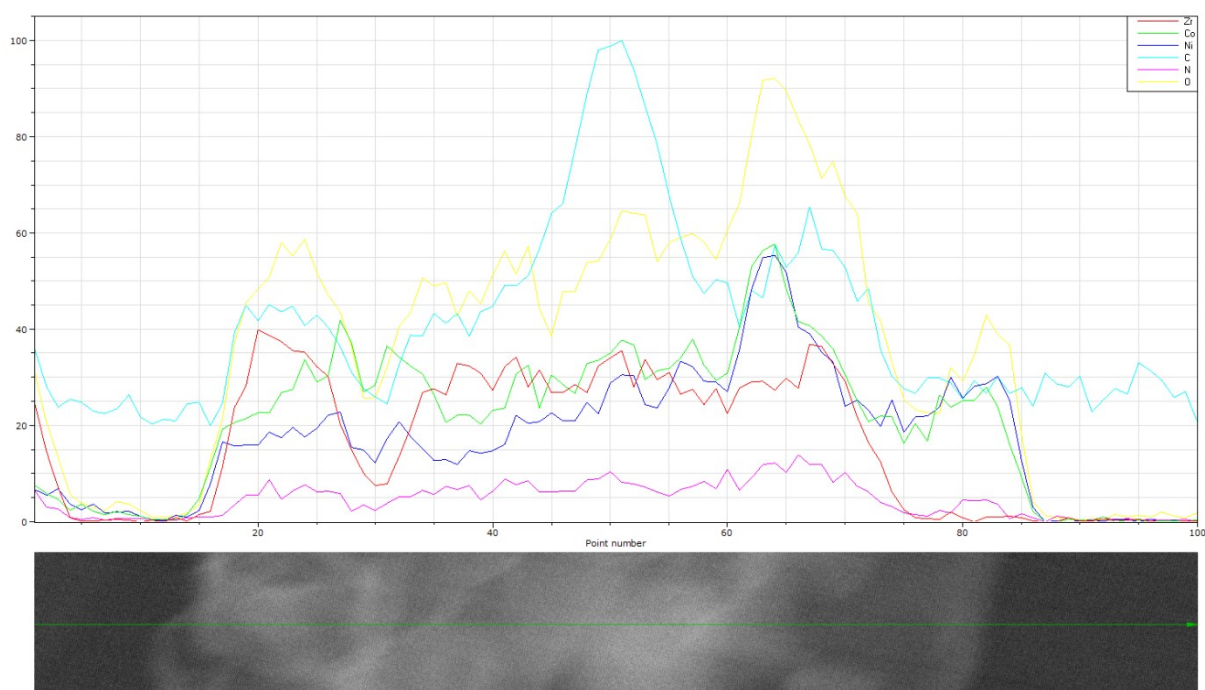


Figure S7. Line profile of NiCo-LDH@NH₂-UiO-66.

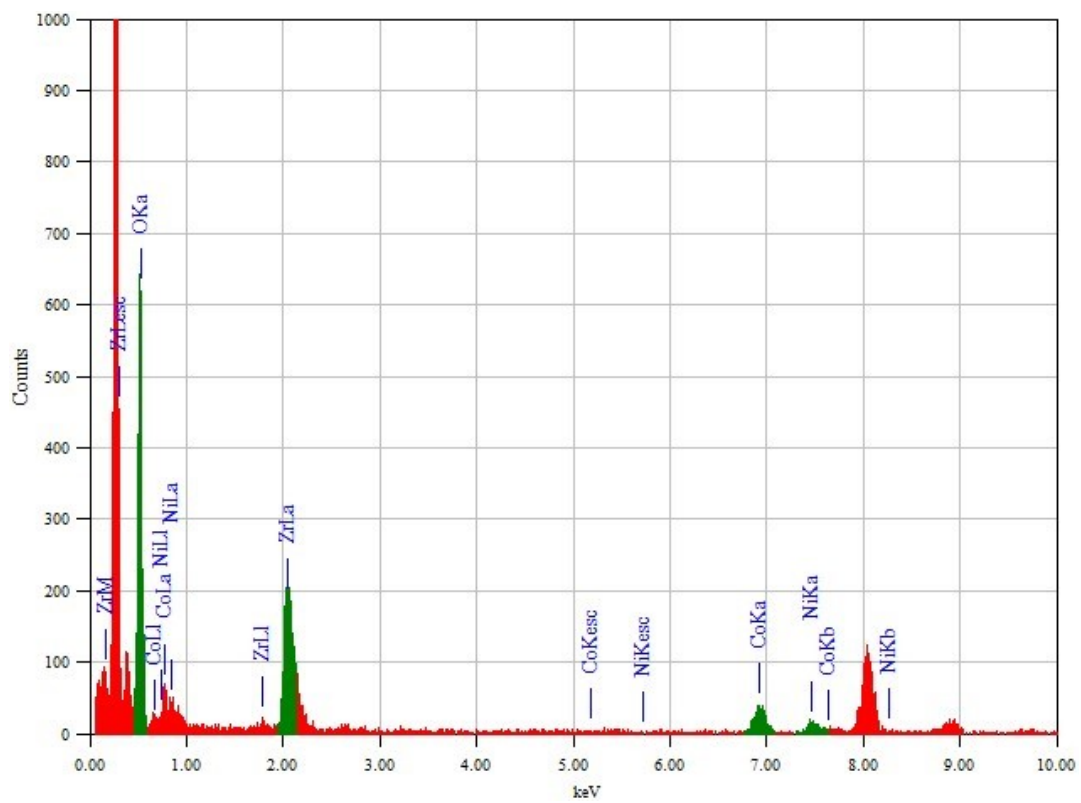


Figure S8. EDX profile of NiCo-LDH@NH₂-UiO-66.

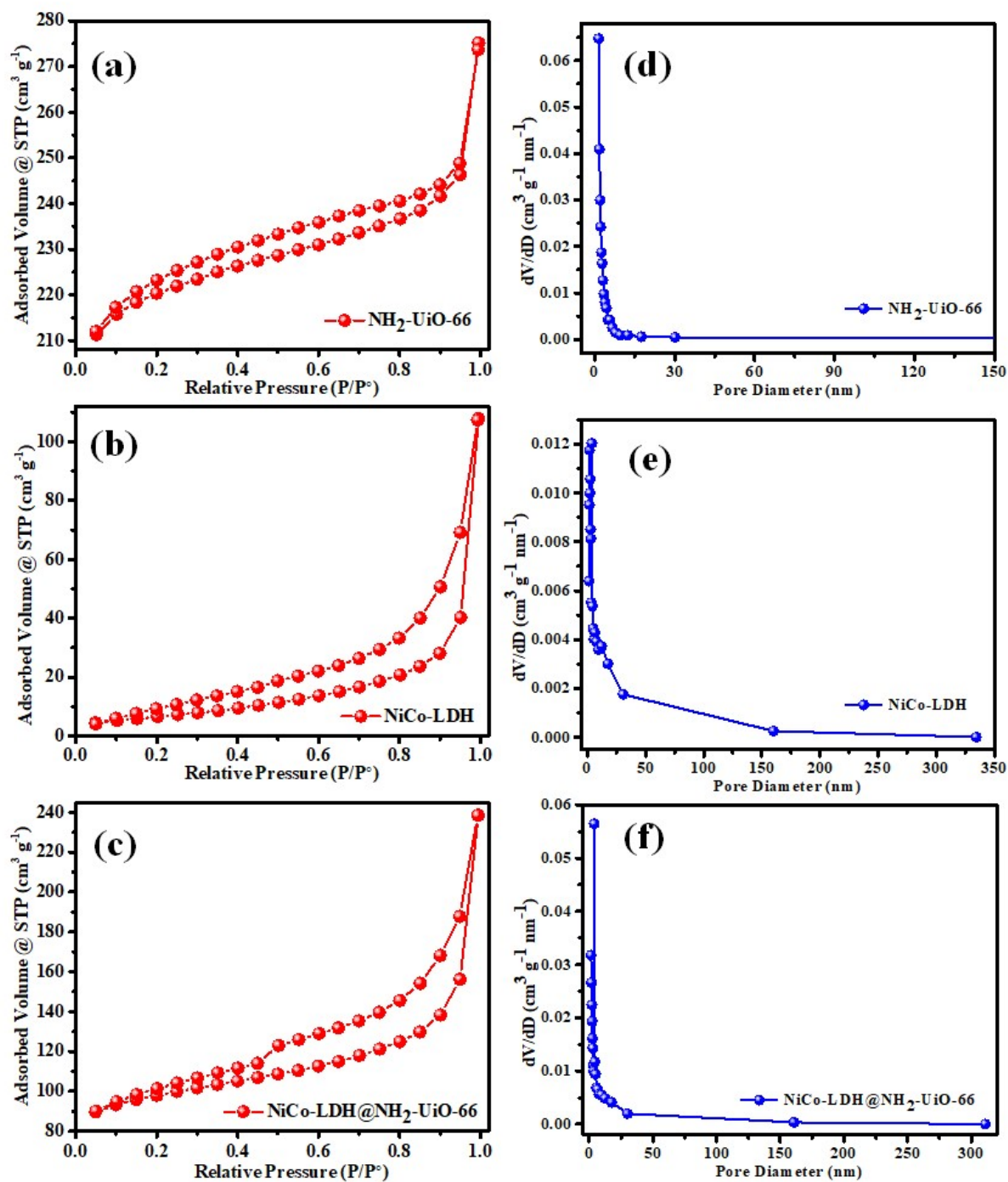


Figure S9. (a-c) N_2 adsorption-desorption isotherms, (d-f) pore size distribution curves of the as-synthesized NH_2 -UiO-66, NiCo-LDH, and NiCo-LDH@ NH_2 -UiO-66 catalysts.

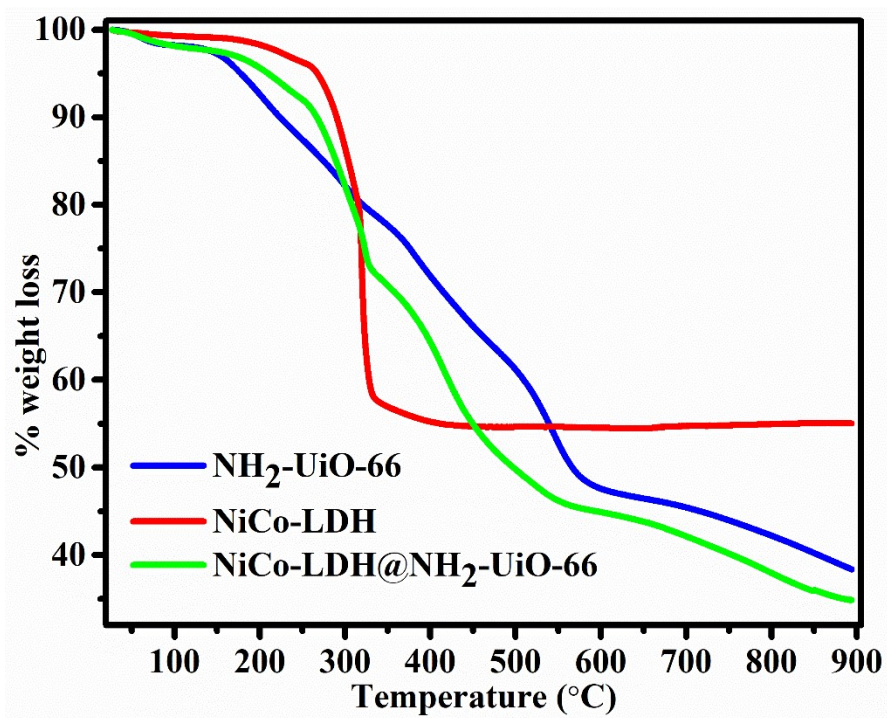


Figure S10. TGA curves under a flow of N₂ at a heating rate of 10 °C min⁻¹.

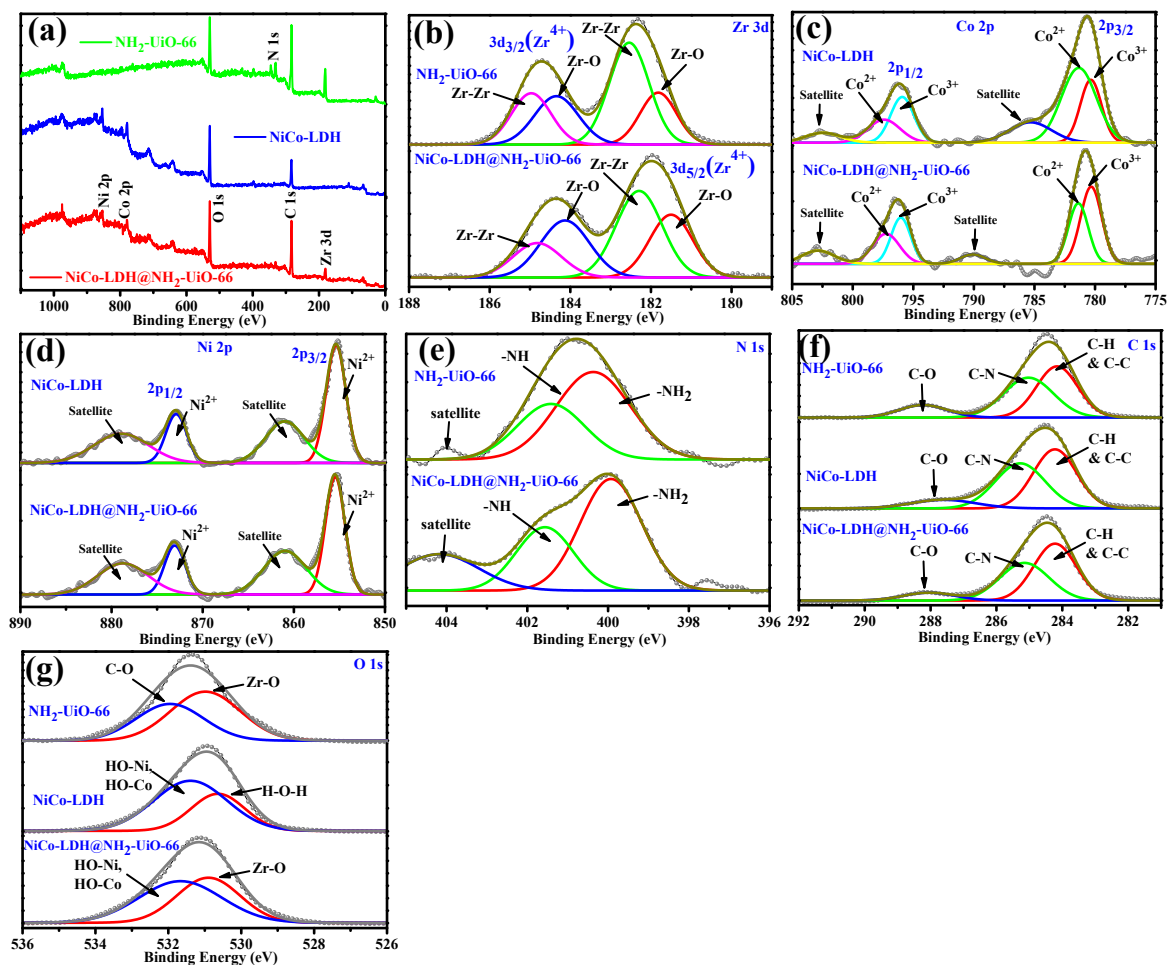


Figure S11. (a) XPS full scan survey spectra of the as-synthesized catalysts. High resolution XPS spectra of (b) Zr 3d, (c) Co 2p, (d) Ni 2p, (e) N 1s, (f) C 1s, and (g) O 1s of NH₂-UiO-66, NiCo-LDH, and NiCo-LDH@NH₂-UiO-66 catalyst.

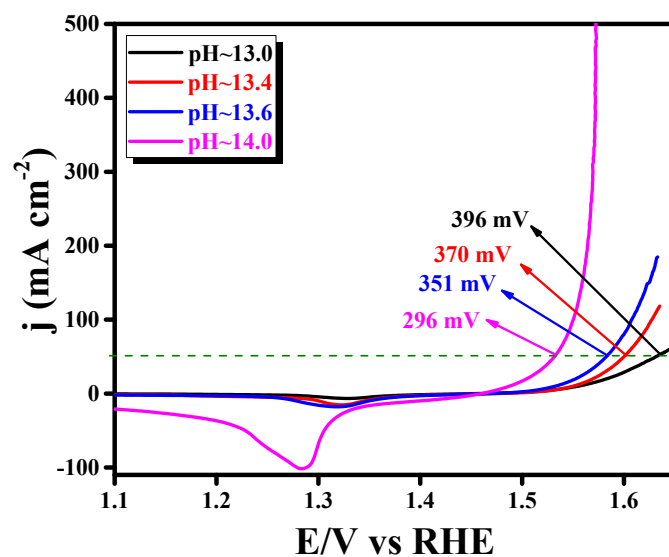


Figure S12. Represents the pH dependent electrocatalytic activity of NiCo-LDH@NH₂-UiO-66 catalyst towards OER at four different pH~13.0, 13.4, 13.6, 14 condition.

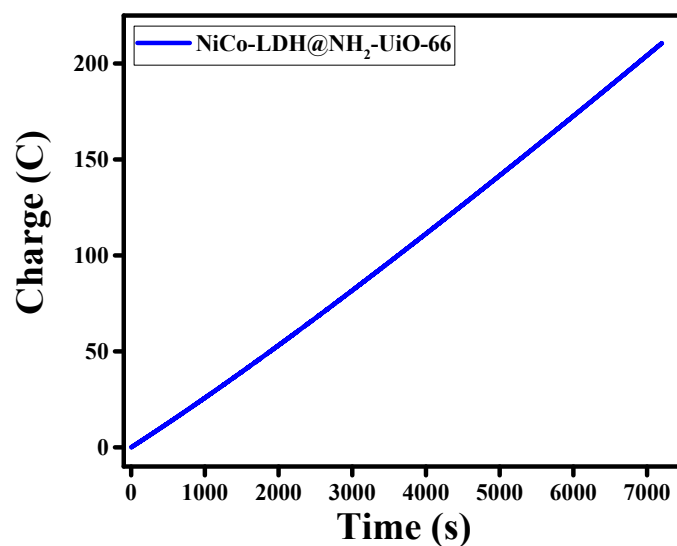


Figure S13. Chronocoulometric study of NiCo-LDH@NH₂-UiO-66 catalyst for 2h towards OER in 1 M KOH.

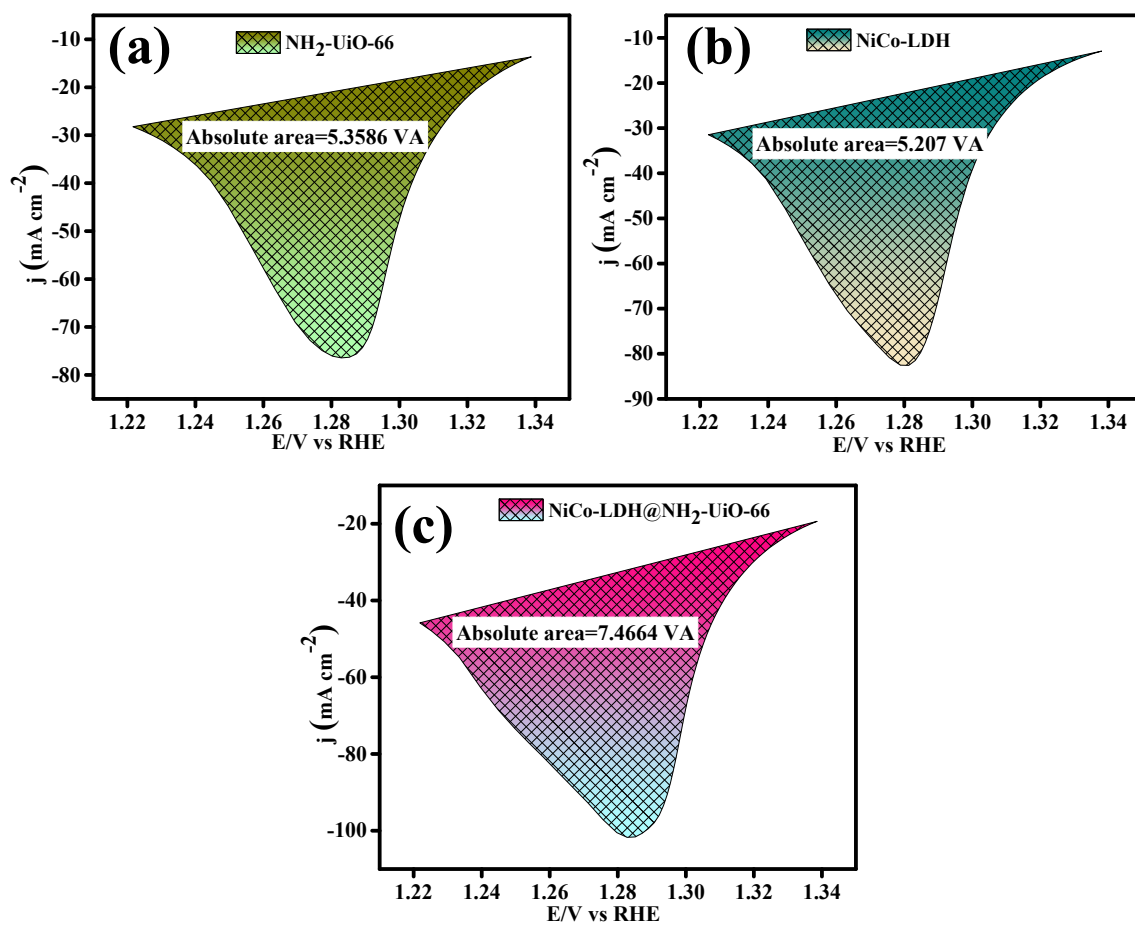


Figure S14. (a-c) are the reduction area peaks for $\text{NH}_2\text{-UiO-66}$, NiCo-LDH and $\text{NiCo-LDH@NH}_2\text{-UiO-66}$, respectively.

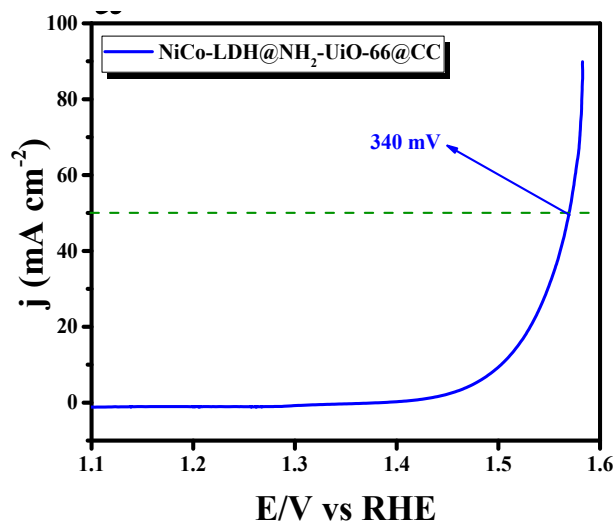


Figure S15. The LSV polarization results of NiCo-LDH@NH₂-UiO-66 catalyst performed in a carbon cloth (CC) substrate.

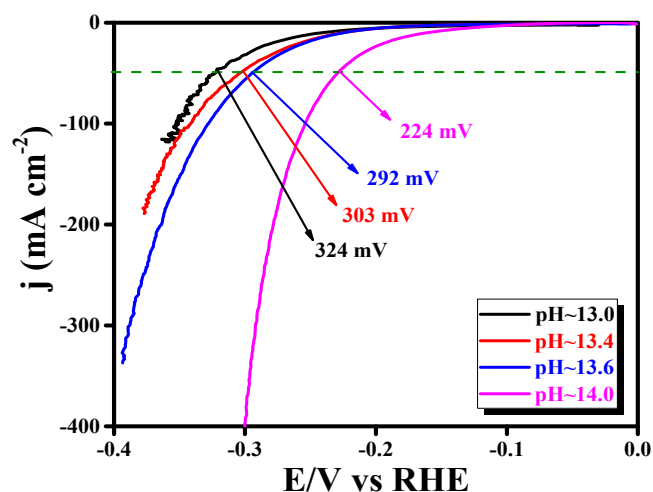


Figure S16. Represents the pH dependent electrocatalytic activity of NiCo-LDH@NH₂-UiO-66 catalyst towards HER at four different pH~13.0, 13.4, 13.6, 14 environment.

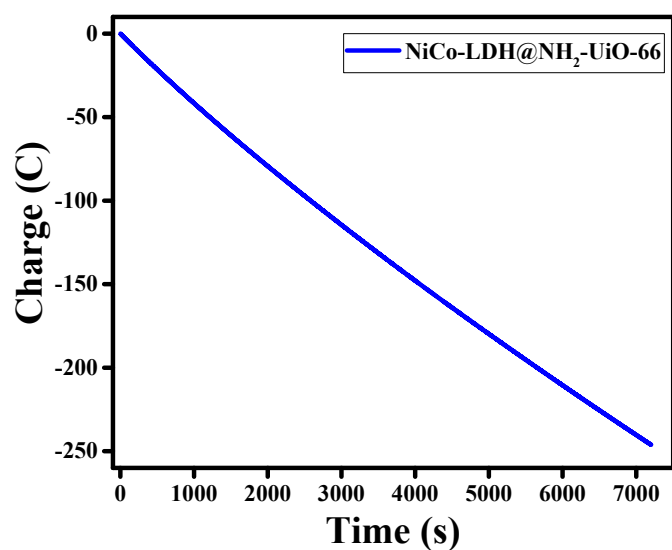


Figure S17. Chronocoulometric study of NiCo-LDH@NH₂-UiO-66 catalyst for 2h towards HER in 1 M KOH.

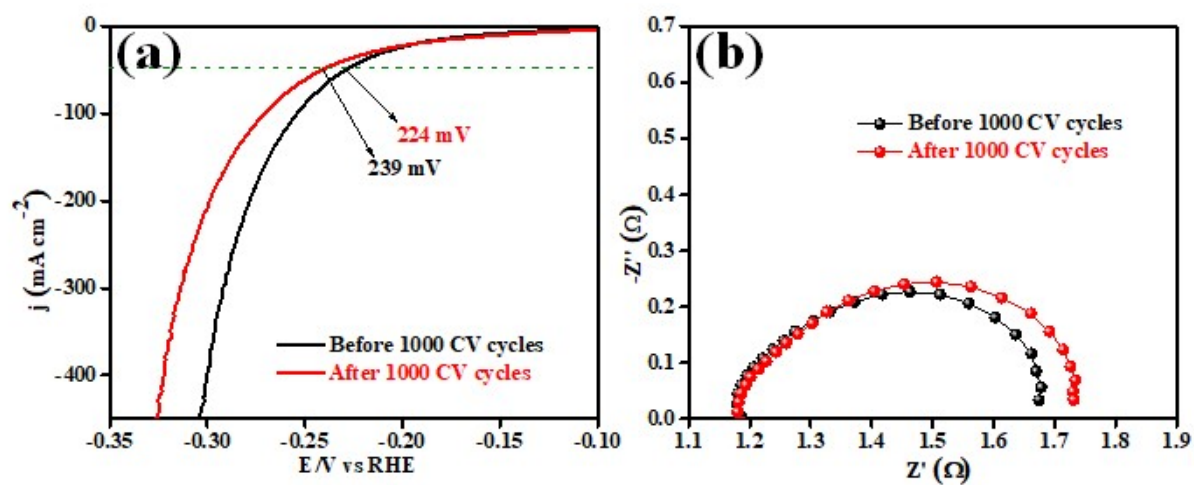


Figure S18. (a) LSV curve of acceleration degradation (AD) study after 1000 cycles for HER, (b) corresponding EIS spectra in 1 M KOH electrolyte solution.

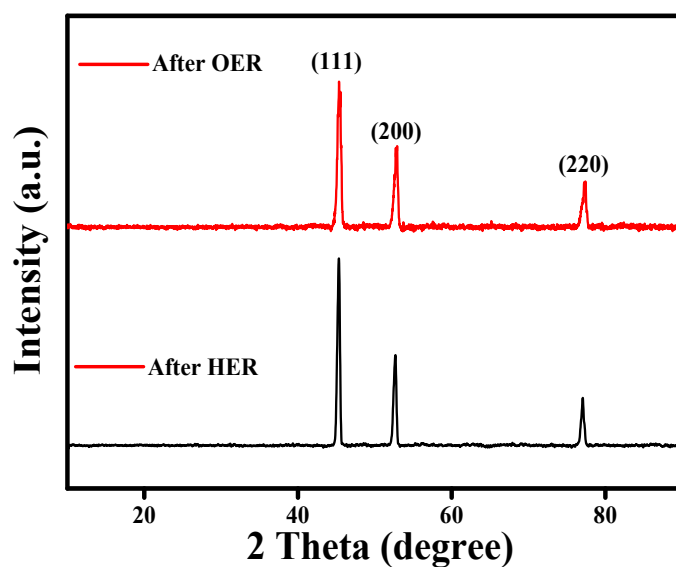


Figure S19. XRD analysis of NiCo-LDH@NH₂-UiO-66 catalyst after electrocatalytic HER and OER process.

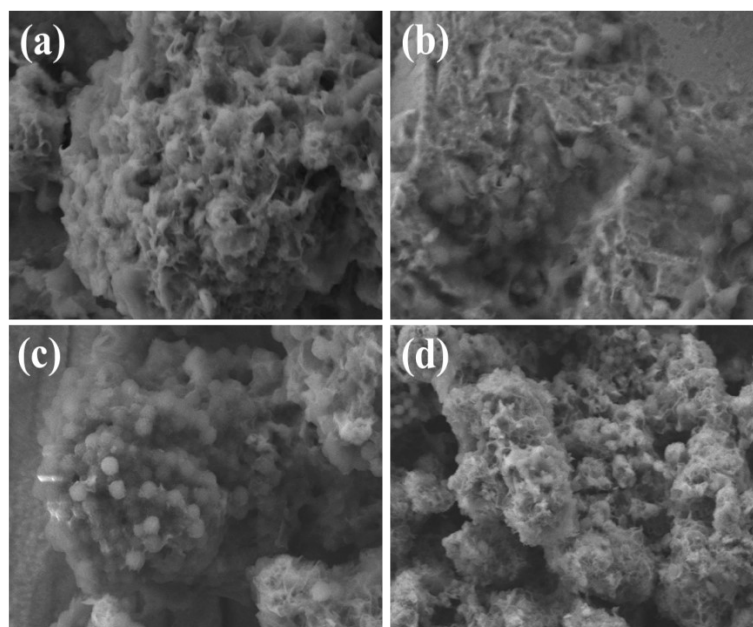


Figure S20. FE-SEM images of NiCo-LDH@NH₂-UiO-66 catalyst after electrocatalytic (a, b) OER and (c, d) HER process in 1 M KOH electrolyte solution.

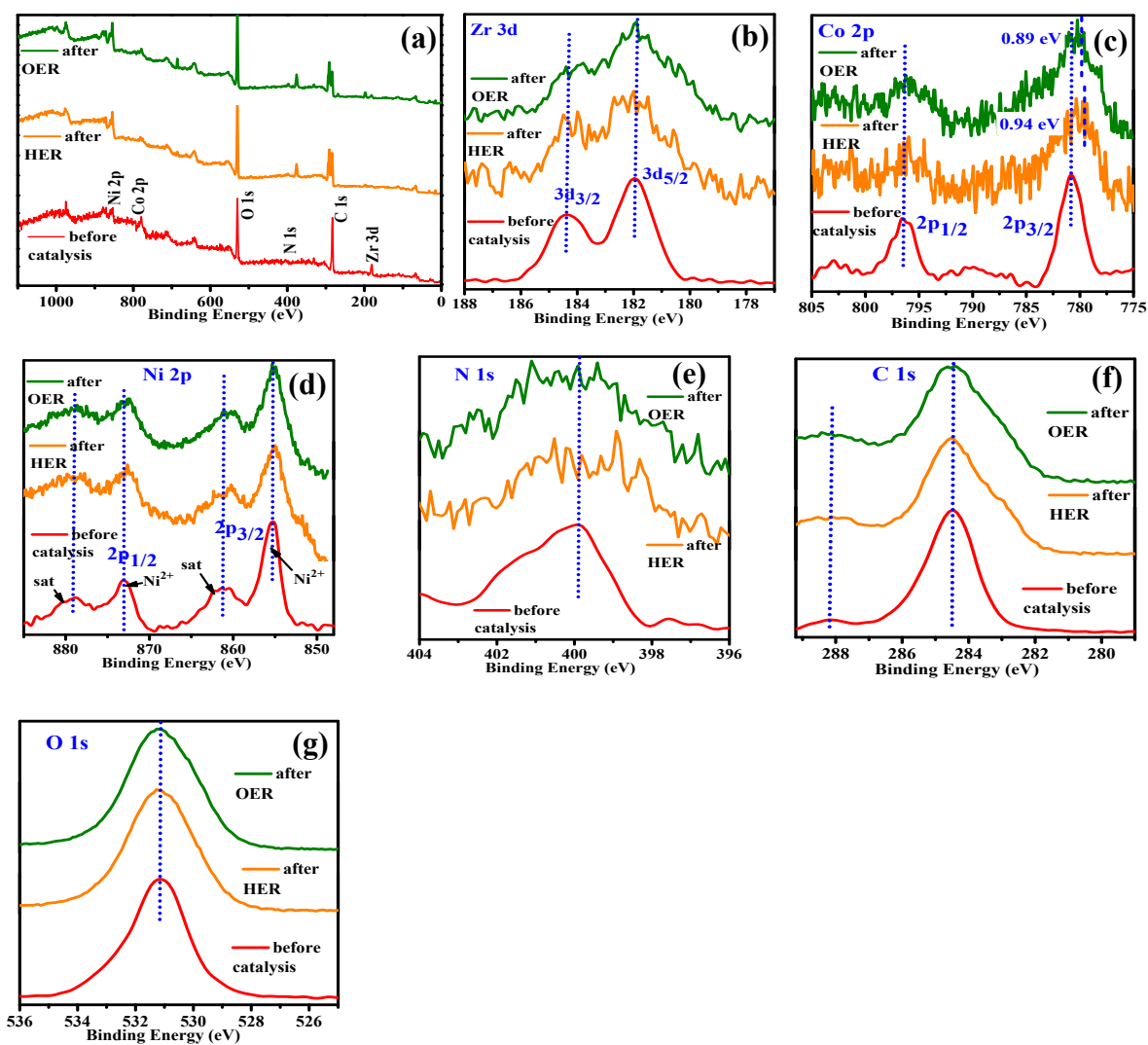


Figure S21. XPS spectra of NiCo-LDH@NH₂-UiO-66 catalyst before and after electrocatalytic HER and OER: (a) full scan survey spectra, (b) Zr 3d, (c) Co 2p, (d) Ni 2p, (e) N 1s, (f) C 1s, and (g) O 1s.

Reference

1. Xiao, J.-D.; Shang, Q.; Xiong, Y.; Zhang, Q.; Luo, Y.; Yu, S.-H.; Jiang, H.-L., Boosting Photocatalytic Hydrogen Production of a Metal–Organic Framework Decorated with Platinum Nanoparticles: The Platinum Location Matters. *Angewandte Chemie International Edition* **2016**, *55* (32), 9389-9393.
2. Wang, T.; Zhang, S.; Yan, X.; Lyu, M.; Wang, L.; Bell, J.; Wang, H., 2-Methylimidazole-Derived Ni–Co Layered Double Hydroxide Nanosheets as High Rate Capability and High Energy Density Storage Material in Hybrid Supercapacitors. *ACS Applied Materials & Interfaces* **2017**, *9* (18), 15510-15524.
3. Poswal, A. K.; Agrawal, A.; Yadav, A. K.; Nayak, C.; Basu, S.; Kane, S. R.; Garg, C. K.; Bhattachryya, D.; Jha, S. N.; Sahoo, N. K., Commissioning and first results of scanning type EXAFS beamline (BL-09) at INDUS-2 synchrotron source. in *AIP Conference Proceedings, American Institute of Physics* **2014**, *1591* (1), 649-651.
4. Basu, S.; Nayak, C.; Yadav, A. K.; Agrawal, A.; Poswal, A. K.; Bhattacharyya, D.; Jha, S. N.; Sahoo, N. K., A comprehensive facility for EXAFS measurements at the INDUS-2 synchrotron source at RRCAT, Indore, India. *Journal of Physics: Conference Series* **2014**, *493*, 012032.
5. Bunker, G., *Introduction to XAFS: A Practical Guide to X-ray Absorption Fine Structure Spectroscopy*. Cambridge University Press: Cambridge, 2010.
6. Kelly, S.; Hesterberg, D.; Ravel, B. J. M. o. s. a. P. M. m., Analysis of soils and minerals using X-ray absorption spectroscopy. *Methods of soil analysis* **2008**, *5*, 387-464.
7. Koningsberger, D. C.; Prins, R., X-ray absorption: principles, applications, techniques of EXAFS, SEXAFS and XANES. *X-Ray Absorption: Principles, Applications, Techniques of EXAFS, SEXAFS and XANES*, Wiley, New York **1987**.
8. Ravel, B.; Newville, M., ATHENA, ARTEMIS, HEPHAESTUS: data analysis for X-ray absorption spectroscopy using IFEFFIT. *Journal of Synchrotron Radiation* **2005**, *12* (4), 537-541.
9. Kresse, G.; Furthmüller, J., Efficiency of ab-initio total energy calculations for metals and semiconductors using a plane-wave basis set. *Computational Materials Science* **1996**, *6* (1), 15-50.
10. Perdew, J. P.; Burke, K.; Ernzerhof, M., Generalized Gradient Approximation Made Simple. *Physical Review Letters* **1996**, *77* (18), 3865-3868.
11. Blöchl, P. E., Projector augmented-wave method. *Physical Review B* **1994**, *50* (24), 17953-17979.
12. Grimme, S., Semiempirical GGA-type density functional constructed with a long-range dispersion correction. *Journal of Computational Chemistry* **2006**, *27* (15), 1787-1799.
13. Liu, Y.; Bai, Y.; Yang, W.; Ma, J.; Sun, K., Self-supported electrode of NiCo-LDH/NiCo₂S₄/CC with enhanced performance for oxygen evolution reaction and hydrogen evolution reaction. *Electrochimica Acta* **2021**, *367*, 137534.
14. Liu, W.; Bao, J.; Guan, M.; Zhao, Y.; Lian, J.; Qiu, J.; Xu, L.; Huang, Y.; Qian, J.; Li, H., Nickel–cobalt-layered double hydroxide nanosheet arrays on Ni foam as a bifunctional electrocatalyst for overall water splitting. *Dalton Transactions* **2017**, *46* (26), 8372-8376.
15. Que, R.; Liu, S.; Yang, Y.; Pan, Y., Core-shell structure Co₃O₄@NiCo LDH was used as a high efficiency catalyst for overall water splitting. *Materials Letters* **2021**, *288*, 129364.
16. Yan, J.; Chen, L.; Liang, X., Co₉S₈ nanowires@NiCo LDH nanosheets arrays on nickel foams towards efficient overall water splitting. *Science Bulletin* **2019**, *64* (3), 158-165.
17. Xu, X.; Su, L.; Zhang, Y.; Dong, L.; Miao, X., Hierarchical tube brush-like Co₃S₄@NiCo-LDH on Ni foam as a bifunctional electrocatalyst for overall water splitting. *New Journal of Chemistry* **2021**, *45* (34), 15429-15436.

18. Xu, X.; Zhong, W.; Zhang, L.; Liu, G.; Xu, W.; Zhang, Y.; Du, Y., NiCo-LDHs derived NiCo₂S₄ nanostructure coated by MoS₂ nanosheets as high-efficiency bifunctional electrocatalysts for overall water splitting. *Surface and Coatings Technology* **2020**, *397*, 126065.
19. Zhang, L.; Peng, J.; Yuan, Y.; Zhang, W.; Peng, K., Bifunctional heterostructure NiCo-layered double hydroxide nanosheets/NiCoP nanotubes/Ni foam for overall water splitting. *Applied Surface Science* **2021**, *557*, 149831.
20. Jia, L.; Du, G.; Han, D.; Hao, Y.; Zhao, W.; Fan, Y.; Su, Q.; Ding, S.; Xu, B., Ni₃S₂/Cu–NiCo LDH heterostructure nanosheet arrays on Ni foam for electrocatalytic overall water splitting. *Journal of Materials Chemistry A* **2021**, *9* (48), 27639-27650.
21. Dhandapani, H. N.; Mahendiran, D.; Karmakar, A.; Devi, P.; Nagappan, S.; Madhu, R.; Bera, K.; Murugan, P.; Babu, B. R.; Kundu, S., Boosting of overall water splitting activity by regulating the electron distribution over the active sites of Ce doped NiCo–LDH and atomic level understanding of the catalyst by DFT study. *Journal of Materials Chemistry A* **2022**, *10* (34), 17488-17500.
22. Bera, K.; Karmakar, A.; Kumaravel, S.; Sam Sankar, S.; Madhu, R.; N Dhandapani, H.; Nagappan, S.; Kundu, S., Vanadium-Doped Nickel Cobalt Layered Double Hydroxide: A High-Performance Oxygen Evolution Reaction Electrocatalyst in Alkaline Medium. *Inorganic Chemistry* **2022**, *61* (10), 4502-4512.